




Development of Multi-Functional Coating for Ferritic Steels Using Cathodic Plasma Electrolytic Nitriding

RAMACHANDRAN CHELLAPPANDIAN,¹ GEETISUBHRA JENA,¹
LAKSHMAN NEELAKANTAN,^{2,3} and ILAKSH ADLAKHA ^{1,4}

1.—Department of Applied Mechanics, Indian Institute of Technology Madras, Chennai 600036, India. 2.—Department of Metallurgical and Materials Engineering, Indian Institute of Technology Madras, Chennai 600036, India. 3.—e-mail: nlakshman@iitm.ac.in. 4.—e-mail: ilaksh.adlakha@iitm.ac.in

Cathodic plasma electrolytic nitriding (c-PEN) technique has been utilized to modify a low-alloy ferritic steel (2.25Cr-1Mo) surface and assess the effect of the c-PEN layer on corrosion, hydrogen permeation, and tribological behavior of the steel. The surface morphology and phase composition of the c-PEN-treated surface were analyzed, and it was found that the surface exhibits a globular network morphology of iron nitride and expanded ferrite. The potentiodynamic polarization results showed that the c-PEN treatment created an electrochemically noble surface compared to the untreated steel. Next, electrochemical hydrogen permeation experiments carried out on the nitrated surface exhibited a noticeable drop in hydrogen permeability, diffusivity, and reversible trap density of the steel. Furthermore, based on nanomechanical and tribological characterization, the c-PEN treatment was found to create a noticeably harder and wear-resistant surface. Overall, these findings demonstrate the applicability of c-PEN treatment to create a multi-functional coating for low-alloy steels that can assist in mitigating the effect of various harsh environments.

INTRODUCTION

Low-alloy steels (LAS) are a broad family of steels that contain a small amount (< 5 wt.%) of alloying additions (i.e., Cr, Mo, Ni, V, etc.) and a maximum carbon content of 0.2 wt.% that find applications across various sectors, such as aerospace, automobile, nuclear, petroleum, and shipping.^{1–4} This exposes the LAS to a wide range of operating conditions that can degrade their functional properties. For instance, in the petroleum and shipping industries, the LASs are utilized in harsh marine conditions for a prolonged duration, thus necessitating that the steel exhibits excellent resistance to corrosion and hydrogen embrittlement.^{5–7} This is an issue with LASs because the microstructure primarily consists of the ferritic phase, which is widely known to demonstrate a high degree of

susceptibility to corrosion and hydrogen embrittlement.^{5–7} For instance, the passivation layer formed above the LAS can be easily damaged in chloride-rich environments (marine environments), enabling continuous corrosion of the steel.⁵ Similarly, the ingress of hydrogen can take place when the steel is exposed to a hydrogen-rich environment.^{6,7} This leads to the hydrogen reduction at the steel surface, and a portion of the reduced hydrogen is adsorbed at the surface that readily diffuses towards microstructural defects, and the subsequent accumulation of hydrogen can lead to a noticeable drop in mechanical behavior.^{1,2} In certain applications, such as metal forming, railway undercarriages, and aircraft landing gears, the repeated/continuous contact with abrasive surfaces can lead to wear that can compromise the structural integrity of the component.⁸ The ability of LASs to withstand corrosion, hydrogen embrittlement, and wear can be mainly achieved in two ways: (1) engineering microstructure/alloy,^{9–13} and (2) surface modification methods.^{14–16} However, engineering the

(Received March 21, 2023; accepted June 27, 2023; published online July 13, 2023)

microstructure to mitigate corrosion, hydrogen embrittlement, and wear in LASs brings in additional costs and limited enhancements.^{9–13} On the other hand, surface modification techniques, such as plasma nitriding, thermal spray deposition, and shot peening, address these issues in a cost-effective manner.^{14–16}

The plasma nitriding process exposes the substrate surface to a nitrogen gas mixture that is used as the nitrogen source while applying a high DC voltage (~ 500 V) and maintaining the substrate temperature around 500°C . This causes the ionized N atoms to become adsorbed at the substrate surface and to form a nitride layer on the substrate surface. This is a widely used surface modification technique to address corrosion, wear, and hydrogen permeation in steels, owing to the negligible substrate deformation, good adhesion properties, and mass-scale capabilities.^{16–22} For instance, plasma nitriding on AISI 420 steel at 450°C was found to create a nitride layer that exhibited a lower corrosion current density compared to the untreated surface.¹⁶ Furthermore, the potentiodynamic polarization revealed a wider passivation region due to the presence of the nitrided layer,¹⁶ thus quantifying the improvement in corrosion behavior for nitrided steel specimens. Similarly, corrosion resistance was observed for plasma-nitrided AISI 4140 steel at 600°C for 4 h,¹⁸ thus highlighting the potential of plasma nitriding to provide corrosion resistance across different steels. Additionally, the surface modification achieved with the help of plasma nitriding also exhibited improved wear resistance on steels due to the formation of a harder nitride layer that retarded wear damage.^{18,19}

The presence of nitrides, carbides, oxides, aluminides, etc. is an effective means for trapping hydrogen, as hydrogen atoms find these intermetallics to be energetically favorable trapping sites,²³ thereby reducing the hydrogen concentration within the steel to cause hydrogen embrittlement. Based on this concept, the use of a plasma-nitriding process to deposit a nitride-rich layer as a hydrogen barrier coating to alleviate the hydrogen embrittlement issue across various steels has shown promising results.^{20–22} For instance, the apparent hydrogen diffusivity obtained by performing hydrogen permeation experiments across nitrided AISI 4140 steel ($0.053\text{--}0.19 \times 10^{-6} \text{ cm}^2/\text{s}$) was two orders lower than untreated steels ($1.7\text{--}1.9 \times 10^{-6} \text{ cm}^2/\text{s}$).²⁰ However, the low energy utilization, high cost, and long process time associated with plasma nitriding can be overcome by utilizing the plasma electrolytic nitriding process.^{24–31} In the plasma electrolytic nitriding process, plasma is created by applying voltage between two metal electrodes in the presence of an aqueous nitrogen-rich electrolyte. The plasma ionizes nitrogen from the electrolyte, which then becomes part of the plasma envelope above the active electrode and reacts with the electrode surface to form a nitride layer. There have

been past studies that demonstrated the ability of the plasma electrolytic nitriding process to enhance the wear and corrosion resistance of ferrous alloys,^{28–31} but the effectiveness of this technique to mitigate hydrogen permeation has not been examined.

In this work, we focus on the development of multi-functional coatings for a commercial LAS (2.25Cr-1Mo) using the cathodic plasma electrolytic nitriding (c-PEN) process. First, microstructure analysis of the nitride layer formed using c-PEN treatment was carried out to understand the composition and thickness using XRD, SEM, and EDS techniques. It was found that, using the c-PEN treatment, a nitride layer was successfully formed on the steel substrate. Next, the electrochemical behavior of the c-PEN treated steel was examined with the help of potentiodynamic polarization and electrochemical impedance spectroscopy (EIS). Furthermore, the effect of the nitrided layer on the hydrogen permeation behavior was thoroughly examined. Lastly, the mechanical and tribological properties of the nitride coating were assessed using nanoindentation and ball-on-disc wear tests. Overall, these findings provide insights into the viability of c-PEN treatment for creating multi-functional coatings on LAS.

EXPERIMENTAL

Material

Plates of 2.25Cr-1Mo steel (ASTM A387, Grade 22; 5 mm thick) were used as specimen material for the present study. The chemical composition of the 2.25Cr-1Mo steel was estimated using optical emission spectroscopy and is tabulated in Table I.

The steel plates were normalized by heat treating at 1193 K for 1 h, followed by air-cooling, and then used as the base material for cathodic plasma electrolytic nitriding (c-PEN).

Cathodic Plasma Electrolytic Nitriding Treatment

Normalized steel specimens of size $100 \text{ mm} \times 25 \text{ mm} \times 5 \text{ mm}$ were cut using an electrical discharge machining for the c-PEN process. These specimens were further polished using SiC abrasive papers up to 800 grit, followed by degreasing with acetone and ethanol, and finally dried at ambient temperature. The c-PEN process was carried out in an aqueous solution prepared by adding 543 g of urea (NH_2CONH_2), 10 g of polyethylene glycol (MW-2000), and 16.7 g of ammonium chloride (NH_4Cl) to 1 L of double-distilled water. The electrolytes were further mixed using a magnetic stirrer to ensure a homogenous solution. Subsequently, the solution was transferred to the inner compartment of a double-walled cell, and the temperature was maintained at 10°C using a thermostat throughout the process. For the c-PEN treatment, the steel

Table I. Chemical composition of 2.25Cr-1Mo steel

Element	C	Mn	P	S	Si	Cr	Mo	Fe
Wt. %	0.116	0.624	0.012	0.003	0.412	2.490	0.888	Bal.

specimens with an exposed area of 4 cm² were used as the cathode, and platinum foil was used as the anode. The voltage between the electrodes was ramped up from 50 V to 220 V at a rate of 1 V/s. The nitriding process was carried out for 10 min after attaining the peak voltage (220 V), as reported elsewhere.²⁹

Microstructural Characterization

Specimens were cut from the c-PEN-treated steel to conduct further characterization studies. X-ray diffraction (XRD) analysis was performed to determine the phase compositions of the c-PEN-treated layer using Cu-K α radiation ($\lambda = 1.54 \text{ \AA}$) in the 2θ range of 30°–90°. Next, scanning electron microscopy (SEM) was utilized to assess the surface microstructure of the specimens, and their chemical composition was analyzed using energy-dispersive x-ray spectroscopy (EDS) coupled with SEM. A cross-sectional SEM analysis was also carried out to investigate the elemental distribution along the thickness of the specimens. For the cross-sectional SEM analysis, the specimens were polished with 1- μm diamond paste to acquire a mirror-like surface finish and subsequently etched with 2% Nital.

Electrochemical Characterization

The electrochemical behavior of the c-PEN treated specimens was characterized with the help of open circuit potential (OCP), electrochemical impedance spectroscopy (EIS), and potentiodynamic polarization in a 3.5% NaCl solution. A three-electrode cell setup was utilized, where the working electrode was the c-PEN-treated or untreated surface with an exposed area of 0.785 cm², Ag/AgCl (3 M KCl) was the reference electrode, and spiral Pt wire was the counter electrode. The OCP was carried out for a duration of 1 h, followed by EIS analysis of the c-PEN-treated and untreated steel specimens, with a voltage of 0.01 V (RMS) across a range of 100 kHz to 10 mHz. The potentiodynamic polarization curves were also recorded with a scan rate of 10 mV/min in 3.5% NaCl solution in the potential range of $\pm 300 \text{ mV}$ versus the OCP. To ensure reproducibility, each electrochemical experiment was carried out three times.

Hydrogen Permeation

A custom-made double electrolytic cell (Devanathan–Stachurski cell³²) containing two individual three-electrode cells (charging cell and detection cell) was used to carry out the hydrogen permeation

experiments. The test specimens were prepared with the dimensions of 25 mm \times 25 mm \times 1 mm. The test specimens (untreated and c-PEN-treated) were fixed between the cells, with an exposed area of 0.5 cm² acting as a working electrode for both cells. The silver–silver chloride (Ag/AgCl (3 M KCl)) and the platinum wire were used as the reference and counter electrodes. Both cells were filled with 0.1 M NaOH solution and de-aerated with nitrogen (N₂) gas before and during the experiment. The charging side (cathodic side) of the specimen surface was potentiostatically polarized at -1.35 V versus Ag/AgCl, which reduces the hydrogen (H⁺) ions from the electrolyte into atomic hydrogen (H) on the cathodic surface. The atomic hydrogen diffused through the specimen was oxidized during the experiment to measure the hydrogen permeation rate. For this purpose, the detecting side (anodic side) of the specimen surface was potentiostatically polarized at 0 V versus Ag/AgCl, and the corresponding current was measured until it reached a stable background current ($< 0.1 \mu\text{A}$). Then, the hydrogen charging was initiated at the cathodic side and the corresponding oxidation current (permeation current) at the anodic surface was recorded until it reached the steady-state condition (rising transient). After that, the cathodic polarization was interrupted to measure the decaying current until it reached the background current (decay transient). In the case of the c-PEN-treated specimens, the treated surface side was cathodically polarized to perform the hydrogen permeation experiments.

Nanomechanical Characterization

The mechanical properties of the c-PEN-treated steel surface were assessed using a nano-indentation tester. A Berkovich tip was utilized for the indentations with a maximum load of 5 mN. The loading time, dwell time, and unloading time used in this study were 5 s, 2 s, and 5 s, respectively. A total of 5 indentations were made for each specimen, and the corresponding load–displacement (L-D) curves were recorded. The hardness and reduced elastic modulus of the c-PEN-treated steel specimens were calculated from the L-D curves, according to the Oliver–Pharr method.³³

Tribological Characterization

The ball-on-disc wear tests were conducted as per ASTM G99³⁴ on both the c-PEN-treated and untreated specimens at room temperature to obtain the coefficient of friction. In this test, a 5-mm-diameter wear track was made on the specimens at

a sliding velocity of 0.1 m/s for 10 min using an Al_2O_3 ball. Subsequently, the worn surfaces were analyzed using an optical profilometer to find the wear rate (K) with the help of Archard's equation:^{19,35}

$$K = \frac{Q}{WL} = \frac{5\pi D l \sqrt{dl}}{4WL} \left(\frac{\text{mm}^3}{\text{Nm}} \right) \quad (1)$$

where Q is the wear volume (mm^3), d is the diameter of the Al_2O_3 ball (6 mm), D and l are the diameter (mm) and depth (μm) of the wear tracks, respectively, W is the applied normal load during the wear test (N), and L is the total sliding distance of the Al_2O_3 ball (m).

RESULTS AND DISCUSSION

Compositional Analysis

The phase analysis for the c-PEN-treated specimen was carried out by examining the XRD patterns (Fig. 1). The peaks of the untreated specimen indicate the crystallographic planes of (110), (200), and (211), which correspond to the presence of the BCC (ferrite) phase (ICSD 631734) (Fig. 1). The c-PEN-treated specimen shows similar peaks corresponding to the BCC (ferrite) phase, with a slight shift towards lower diffraction angles due to the lattice expansion of ferrite caused by the supersaturation of nitrogen^{29,36} (Fig. 1). Furthermore, the lattice parameter of the nitrated specimen was slightly larger ($a_N = 2.867 \text{ \AA}$), as compared to the untreated BCC phase ($a = 2.855 \text{ \AA}$). A similar lattice expansion was observed for austenitic and ferritic phases in the plasma-nitrated duplex stainless steel by Tschiptschin et al.³⁶ Plausibly, the applied voltage of 220 V during c-PEN produces atomic nitrogen on the steel surface, which diffuses into the BCC lattice leading to lattice expansion.^{16,36} An additional XRD peak was observed in the c-PEN-treated specimen, indicating the presence of a FCC-iron nitride ($\text{FeN}_{0.076}$) phase (Fig. 1), as reported

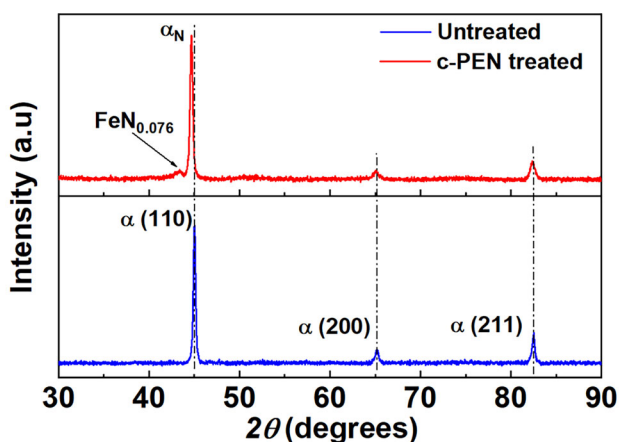


Fig. 1. XRD patterns of the untreated and c-PEN-treated specimens.

elsewhere.^{26,29} By comparing the XRD results of the untreated and c-PEN-treated specimens, it can be demonstrated that the steel surface was modified during the c-PEN process, and that the modified layer contains expanded ferrite and iron nitride (Fig. 1).

Microstructural Analysis

The surface and cross-sectional microstructural features of the c-PEN-treated specimen were analyzed by SEM. Its surface exhibited a globular network morphology (bright globules, connected by the gray-colored branches) (Fig. 2a). This surface morphology was observed due to localized melting of the steel from plasma discharge on the surface. The surface microstructure is consistent with Gui et al.,³⁷ where the c-PEN-treated 304 stainless steel surface exhibited a similar microstructure. The cross-sectional SEM image shows a clear distinction between the substrate and the nitride layer (Fig. 2b). The average nitride layer thickness was measured at 4.41 μm .

The chemical composition of the c-PEN-treated surface was evaluated using EDS analysis at different surface locations indicated in Fig. 2a. In the globular region (spot 2), higher concentrations of nitrogen, carbon, and oxygen were observed compared to the branch region (spot 1) (Fig. 2c). Additionally, the black region (spot 3) was found to be a carbon-rich region on the nitride surface (Fig. 2c). The line EDS analysis along the cross-section of the c-PEN-treated specimen also indicated that the c-PEN layer contains more carbon, nitrogen, and oxygen compared to the base material (Fig. 2d). These results indicate that the globular network is comprised of iron nitride and expanded ferrite with some amounts of carbon and oxygen, and that the black patch region was enriched with carbon. This dispersion of carbon and oxygen in the c-PEN layer is due to the large amount of energy released on the steel surface from the continuous breakdown of plasma bubbles in the electrolyte at higher potential.³⁷ Furthermore, it was found that the diffusion of atomic nitrogen into the ferrite matrix results in compressive residual stress in the modified layer due to the expansion of ferrite.^{16,36} Due to this compressive residual stress, the carbon atoms present in the base material are redistributed and diffused to the stress-free regions, i.e., to the surface and the nitrating facade. This leads to the formation of carbon-rich regions in the nitride layer.³⁸

Electrochemical Analysis

Next, the electrochemical behavior of the c-PEN-treated surfaces was evaluated for electrochemical behavior using DC and AC polarization. The corrosion potential (E_{corr}) and corrosion current density (i_{corr}) were deduced from the potentiodynamic polarization plots (Fig. 3a) using the Tafel extrapolation. The c-PEN treatment was found to result in

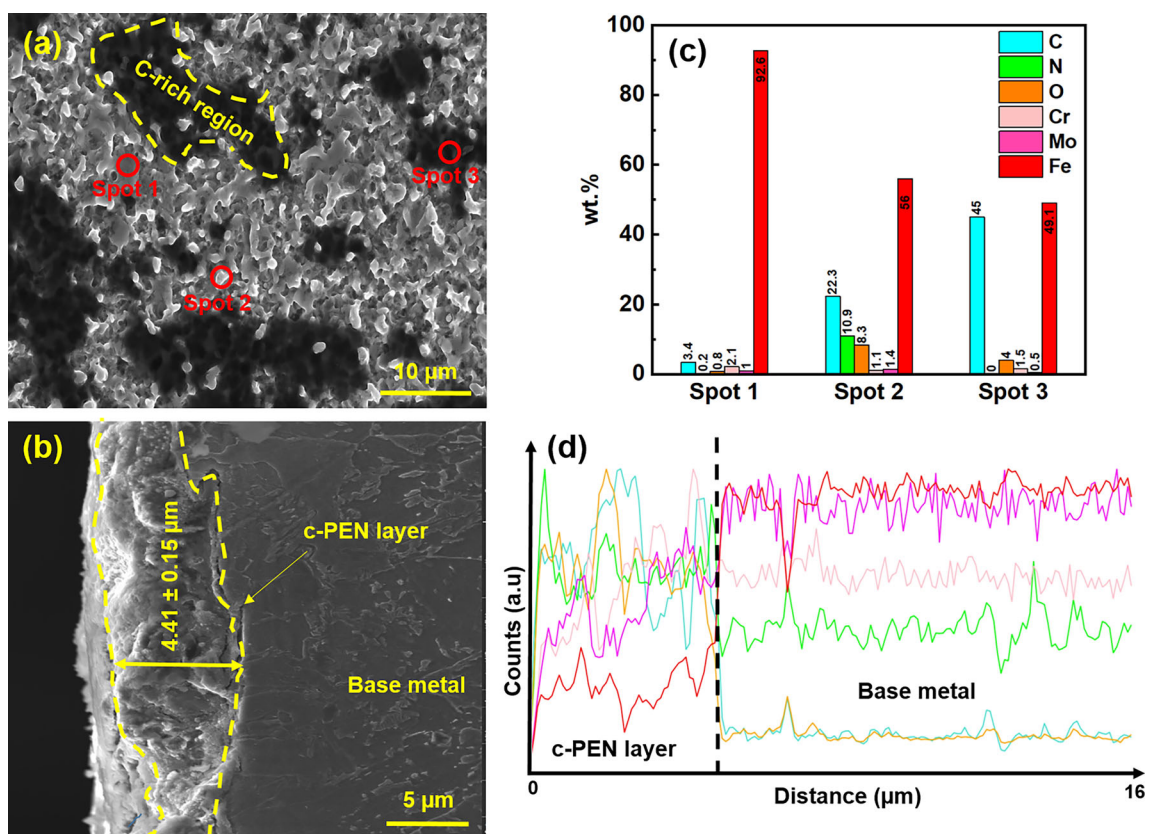


Fig. 2. (a) Surface and (b) cross-sectional SEM micrographs, (c) EDS spectrums of the spots marked in the surface micrograph, (d) line EDS spectrum for the cross-section of the c-PEN-treated specimen.

a nobler surface (-0.47 V) compared to the untreated surface (-0.58 V), based on the obtained corrosion potential (Fig. 3a). This indicates that the nitridation process enhances the corrosion resistance of the modified surface. The corrosion current density (i_{corr}) values of the untreated and c-PEN treated specimens were found to be 26.30 and 25.03 $\mu\text{A cm}^{-2}$, respectively. Even though the corrosion rate is not significantly improved due to the nitridation process, a comparison of the anodic branch of the polarization curves clearly indicates a noticeable drop in the current density observed at the given potential for the nitrided surface. For instance, the current density for the c-PEN-treated specimen at -0.40 V is 0.74 mA cm^{-2} , which is approximately one order lower compared to the untreated specimen (3.79 mA cm^{-2}). Therefore, these findings clearly indicate that the nitridation process retards the anodic dissolution compared to the untreated specimen. The lower current density for the c-PEN-treated specimen highlights the potential of the c-PEN layer for corrosion protection.

The Nyquist plots for both specimens exhibit a single depressed semicircle, indicating the presence of a single equivalent capacitive loop (Fig. 3b). Based on the diameter of the capacitive loop, it was estimated that the c-PEN-treated specimen exhibited better corrosion resistance, as it had a larger

capacitive loop compared to the untreated specimen (Fig. 3b). In the phase angle plot (Fig. 3c), the peak position shifted towards the lower frequency range, and the width of the peak also increased. This is due to the enhanced capacitive behavior of the specimen, resulting in effective corrosion mitigation.

The EIS plots of the untreated and c-PEN-treated specimens show a single capacitive loop, indicating that the c-PEN layer has a non-porous microstructure. Therefore, a single-time constant equivalent electrical circuit (EEC) was used to approximate the EIS data for both specimens with better χ^2 values (Fig. 3d). The parameter, R_S , obtained from the EEC is the resistance offered by the test electrolyte and is associated with the high-frequency behavior of the electrochemical system, whereas R_{ct} and Q_{dl} are identified as the charge transfer resistance and constant phase elements at the interface between the electrolyte and the untreated/c-PEN-treated specimen surfaces, respectively. The constant phase element (Q_{dl}) instead of a pure double-layer capacitor (C_{dl}) has been chosen to address the inhomogeneous charge distribution at the interface of the specimen surface and the electrolyte. The fitting parameters of the EIS equivalent circuits obtained for the untreated and c-PEN-treated specimens are set out in Table II, showing that the Q_{dl} value of the c-PEN-treated specimen was lower than for the

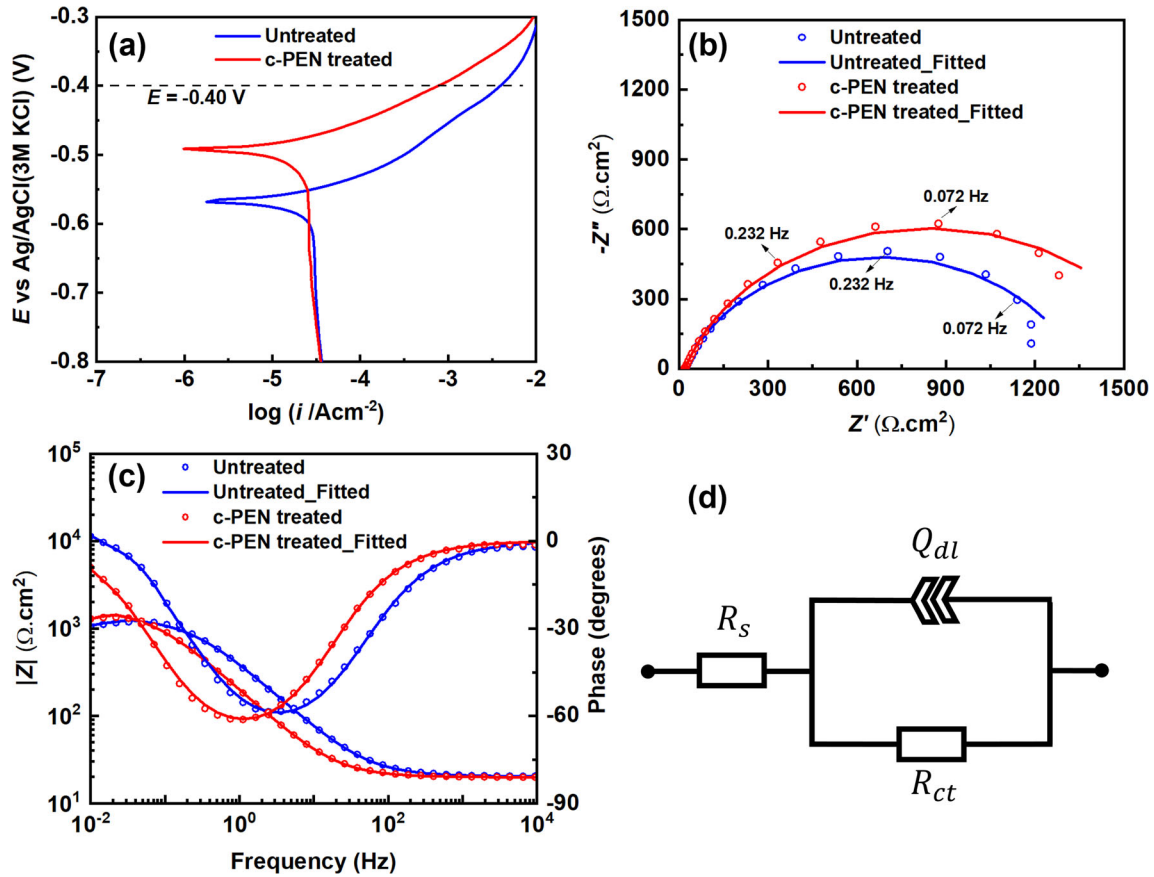


Fig. 3. Representative (a) potentiodynamic polarization plots, (b) Nyquist plots, (c) Bode plots, and (d) the proposed electrical equivalent circuit for the untreated and c-PEN-treated specimens in 3.5% NaCl solution exposed for 1 h at room temperature. R_s , R_{ct} , and Q_{dl} are the resistance offered by the test electrolyte, the charge transfer resistance, and the constant phase elements at the interface between the electrolyte and the untreated/c-PEN-treated specimen surfaces, respectively.

Table II. Electrochemical parameters were obtained from Tafel extrapolation and EIS

Specimen/electrochemical parameters		Untreated	c-PEN-treated
Potentiodynamic polarization	E_{corr} (V vs. Ag/AgCl (3 M KCl))	-0.58 ± 0.03	-0.47 ± 0.02
	i_{corr} ($\mu\text{A cm}^{-2}$)	26.30 ± 1.35	25.03 ± 0.77
EIS	R_s ($\Omega \text{ cm}^2$)	18.09 ± 4.24	16.70 ± 3.12
	R_{ct} ($\Omega \text{ cm}^2$)	1315 ± 13.82	1625 ± 19.53
	$Q_{dl} \times 10^{-3}$ ($\text{F s}^n \text{ cm}^{-2}$)	0.50 ± 0.04	0.14 ± 0.01
	n_{dl}	0.78 ± 0.02	0.79 ± 0.02

untreated specimen, which suggests a smaller amount of ingress of Cl^- species and a negligible accumulation of electric charge on the c-PEN-treated surface. At the same time, the charge transfer resistance of the c-PEN-treated specimen was also found to be higher than for the untreated specimen.

From these results, it is evident that the corrosion resistance of the c-PEN-treated specimen increased in 3.5% NaCl solution. The enhancement of the corrosion resistance performance of the c-PEN-treated specimen could be correlated with the phase composition of the modified surface layer. Zhang

et al.²⁹ also reported that the presence of $\text{FeN}_{0.076}$ in the nitrated layer increases the corrosion resistance of the specimens.

Hydrogen Permeation

Analysis of Rising Transients

The rising transients for untreated and c-PEN-treated specimens recorded during cathodic charging are shown in Fig. 4a. The observed rising transient of the c-PEN-treated specimen shows a considerable drop and shift towards the right compared to an untreated specimen. The initial flat

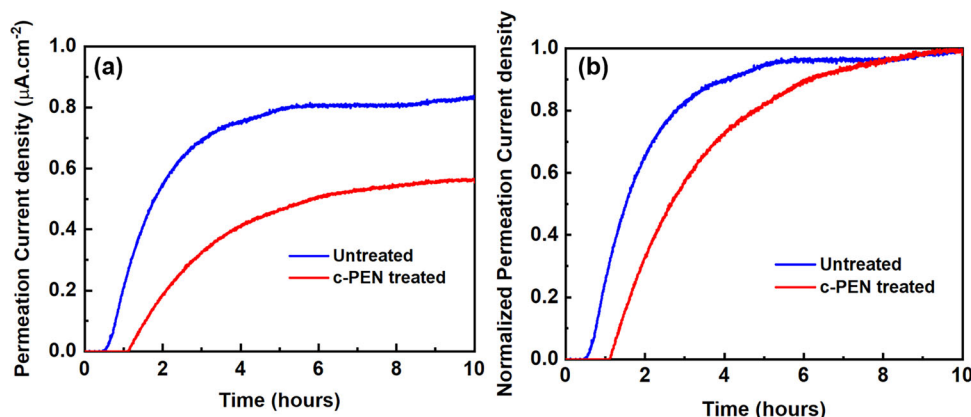


Fig. 4. (a) Experimental permeation rising transients and (b) the corresponding normalized rising transients for untreated and c-PEN-treated 2.25Cr-1Mo steel specimens. Charging conditions: 0.1 M NaOH, -1.35 V versus Ag/AgCl.

region of the rising transient represents the time required for the hydrogen to start exiting from the output side of the specimen. This is called the breakthrough time (t_b), which is two times higher for the c-PEN-treated specimen (4010 s) compared with the untreated specimen (2070 s). It can also be seen that the slope of the normalized rising transient of the untreated specimen is steeper than the c-PEN-treated specimen (Fig. 4b). These results indicate that the c-PEN layer slows down the hydrogen transport. Furthermore, the rising transients were analyzed to quantify the hydrogen permeation parameters, like the steady-state permeation current density (i_{ss}), steady-state hydrogen flux (J_{ss}), permeability ($J_{ss}L$), apparent hydrogen diffusivity (D_{app}), apparent hydrogen concentration/hydrogen solubility (C_{app}), and total H trap density (N_T), which were calculated using:^{39–41}

$$J_{ss} = \frac{i_{ss}}{F} \quad (2a)$$

$$D_{app} = \frac{L^2}{6t_l} \quad (2b)$$

$$C_{app} = \frac{J_{ss}L}{D_{app}} \quad (2c)$$

$$N_T = N_L \left(\frac{D_L}{D_{app}} - 1 \right) e^{\left(\frac{-E_b}{RT} \right)} \quad (2d)$$

where F is the Faraday constant (9.6485×10^4 C mol $^{-1}$), L is the thickness of the specimen, t_l is the time lag (time to achieve a value of 63% of i_{ss}), N_L is the density of interstitial sites (5.1×10^{23} cm $^{-3}$), D_L is the lattice diffusion coefficient of hydrogen in α -Fe (1.28×10^{-4} cm 2 s $^{-1}$), E_b is the trap binding energy (28.9056 kJ mol $^{-1}$), T is the absolute temperature, and R is the gas constant (8.314 kJ mol $^{-1}$).

The hydrogen permeation parameters calculated from the rising transients are set out in Table III.

The apparent diffusivity and permeability of the untreated 2.25Cr-1Mo steel are $D_{app} = 1.87 \times 10^{-7}$ cm 2 s $^{-1}$ and $J_{ss}L = 7.45 \times 10^{-13}$ mol H cm $^{-1}$ s $^{-1}$, which are in close agreement with previously reported studies.^{1,6} From the results reported in Table III, it is certain that the steady-state permeation current density ($i_{ss} = 7.45 \times 10^{-13}$ μ A cm $^{-2}$), permeability ($J_{ss}L = 5.44 \times 10^{-13}$ mol H cm $^{-1}$ s $^{-1}$), and apparent hydrogen diffusivity ($D_{app} = 1.29 \times 10^{-7}$ cm 2 s $^{-1}$) of the c-PEN-treated specimen are lower compared to the untreated specimen. Furthermore, the apparent diffusivity of a c-PEN layer in the c-PEN-treated specimen was found to be two orders lower than the untreated specimen. It can be inferred that the microstructural features of the c-PEN layer impede the H transport and increase the H permeation time.²⁰ The corresponding results are further supported by the higher apparent hydrogen concentration ($C_{app} = 4.20 \times 10^{-6}$ mol H cm $^{-3}$) and total H trap density ($N_T = 5.06 \times 10^{26}$ cm $^{-3}$) of c-PEN-treated specimen. It was reported that nitrogen increases the trapping possibility of hydrogen in austenitic steel due to the accumulation of hydrogen at the expanded lattice due to nitrogen atoms.⁴² Therefore, it can be stated that the presence of expanded ferrite and iron nitride in the c-PEN layer enhances the trapping feasibility of hydrogen. From the results of the lower hydrogen diffusivity and higher trapping ability of the c-PEN-treated specimen, it can be demonstrated that the c-PEN treatment increases the hydrogen permeation barrier performance of the steel.

Analysis of Decay Transients

When the rising transient reaches the steady state during cathodic charging, it is considered that all the traps (reversible and irreversible traps) are occupied by hydrogen. Therefore, hydrogen can easily diffuse through the interstitial lattice sites with minimum disturbance of the trapping/de-trapping phenomenon. Once the cathodic charging is interrupted, the hydrogen from the lattice sites and

Table III. The hydrogen permeation parameters deduced from charging transients

Parameters/specimen	i_{ss} (μ A cm $^{-2}$)	$J_{ss}L \times 10^{-13}$ (mol H cm $^{-1}$ s $^{-1}$)	$D_{app} \times 10^{-7}$ (cm 2 s $^{-1}$)	$C_{app} \times 10^{-6}$ (mol H cm $^{-3}$)	$N_T \times 10^{26}$ (cm $^{-3}$)
Untreated	0.83 ± 0.01	7.45 ± 0.09	1.87 ± 0.23	4.04 ± 0.55	3.49 ± 0.43
c-PEN-treated	0.55 ± 0.09	5.44 ± 0.93	1.29 ± 0.12	4.20 ± 0.33	5.06 ± 0.48

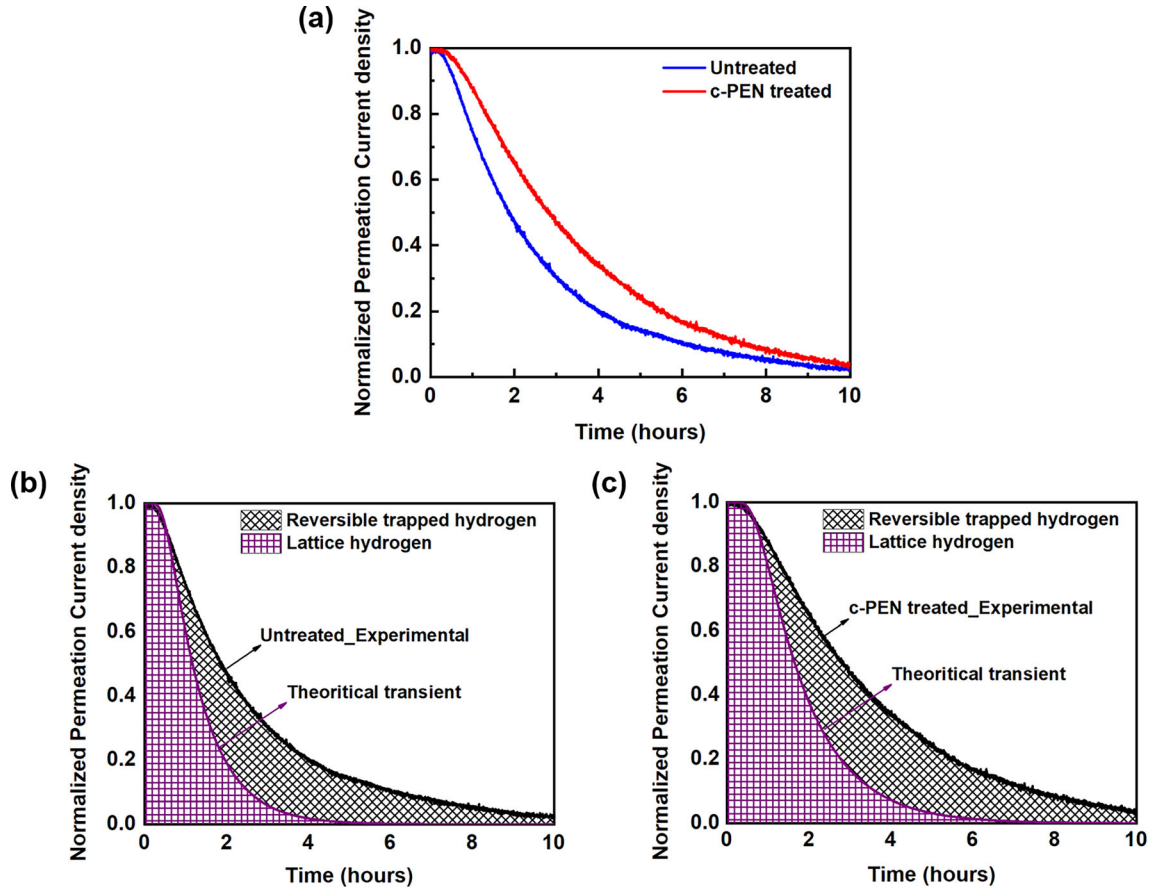


Fig. 5. (a) Experimental decay transients for untreated and c-PEN-treated specimens. Theoretical fitted curve with the experimental decay transients of (b) untreated, (c) c-PEN-treated specimens.

reversible traps start exiting from the output surface. The corresponding permeation transients (decay transient) have been recorded, and the normalized decay transients for untreated and c-PEN-treated specimens are shown in Fig. 5a. The decay transient of the c-PEN-treated specimen shifts towards the right, which indicates the hydrogen desorption rate is reduced due to the c-PEN treatment.

It is known that the dissolved hydrogen concentration can be classified as diffusible hydrogen, which transports through the interstitial sites, and trapped hydrogen, which is trapped in crystalline defects, such as vacancies, dislocations, precipitates, interfaces, and inclusions.⁴³ The microstructural traps which can accommodate interstitial hydrogen

can be further classified into irreversible traps (precipitates, inclusions, and high-angle grain boundaries) and reversible traps (dislocations and low-angle grain boundaries),^{39,43,44} based on the probability of hydrogen escaping from the trap. The ability of hydrogen to diffuse across the lattice is known to play a crucial role in the hydrogen embrittlement of ferritic steels.⁴² The hydrogen concentration within the reversible traps is responsible for providing the readily diffusible hydrogen concentration rather than the hydrogen trapped within irreversible traps.^{43,45} Therefore, the corresponding parameters are calculated by analyzing the decay transients using the following formulations.

The boundary condition at the exit side of the membrane is also common for all transient stages, which means that the hydrogen concentration is equal to zero during the entire experiment $C(t, L) = 0$; The hydrogen concentration distribution across the specimen becomes linear when a steady state is obtained during cathodic charging, $C(x) = C_{\text{app}}(1 - \frac{x}{L})$. Assuming that the concentration drops to zero during the entire decay transient for the boundary condition on the entry side of the membrane, then $C(t, 0) = 0$. It is also assumed that hydrogen is not released from the charging surface. Therefore, the evolution of hydrogen flux for the theoretical decay transient can be expressed as the Laplace solution of the diffusion equation:

$$\frac{j(t)}{j_{\text{ss}}} = 1 - 2 \sum_{n=0}^{\infty} \frac{L}{\sqrt{\pi D_L t}} e^{\left(\frac{-(2n+1)^2 L^2}{4D_L t} \right)} \quad (3a)$$

This is fitted to the experimental results in the initial stages of the decay transient up to 90% of the steady-state current density to obtain the lattice diffusion coefficient (D_L) for high trap occupancy. In this study, $n = 5$ was used to fit with the experimental decay curves as per the ASTM G148⁴⁰ acceptance range ($n = 1-6$), as shown in Fig. 5. The concentration of lattice diffusion-controlled hydrogen (C_{Lattice}) is calculated by integrating the theoretically fitted curve. The trapped hydrogen concentration ($C_{T_{\text{rev}}}$) is calculated by subtracting the concentration of lattice diffusion-controlled hydrogen from the total desorbed hydrogen concentration (C_{diff}), which is determined by integrating the experimental decay transient. Additionally, the reversible trap density ($N_{T_{\text{rev}}}$) of the specimens was found using the permeation curve method:^{39,41}

$$N_{T_{\text{rev}}} = \frac{2s \times i_{\text{ss}} \times 6.24 \times 10^{18}}{L} \quad (3b)$$

where s (A s cm^{-2}) is the area difference between the experimental decay transient and theoretical decay transient with no traps, $1 \text{ A s} = 6.24 \times 10^{18} \text{ e}$ and assuming that each trap holds one hydrogen atom and therefore can be considered as 6.24×10^{18} trap sites.

From the results obtained from the decay transients (Table IV), the lattice diffusion coefficient and the lattice diffusion-controlled hydrogen concentration of the c-PEN-treated specimen are lesser than the untreated specimen. This may be due to the preferential filling of N in the interstitial lattice

sites during the nitriding process, which hinders the H transport and reduces the concentration of diffused H in the interstitial sites.⁴² Additionally, the reversible trap density, reversible trapped hydrogen concentration, and total diffusible hydrogen concentration of the c-PEN-treated specimen are lower than the untreated specimen. It has been well established that the reversible traps are mainly responsible for hydrogen embrittlement in the steels. The reversible trapped hydrogen could have been produced from the decomposition of hydrides or released from the traps, the latter being unstable at ambient temperature. Further, the transport of (trapped) hydrogen is a function of the hydrogen diffusivity of the steel.⁴² Therefore, the lower reversible trapped hydrogen concentration and trap density with less hydrogen diffusivity of the c-PEN-treated specimen indicate the hydrogen embrittlement susceptibility of the steel reduced by c-PEN treatment.^{43,45}

Nanomechanical Properties

The effects of c-PEN on the mechanical properties were examined using the nano-indentation test. The contact depth (h_C) can be related to the mechanical parameters obtained from the nano-indentation test in the following manner. The hardness (H) and reduced elastic modulus (E_r) for the c-PEN-treated and untreated specimens can be derived from the load-displacement curves (Fig. 6) using the following relationships based on the Oliver-Pharr model:³³

$$H = \frac{P_{\text{max}}}{A_C} \quad (4a)$$

$$E_r = \frac{\sqrt{\pi} 1}{2} \frac{S}{\beta \sqrt{A_C}} \quad (4b)$$

where P_{max} is the maximum applied load, and A_C is the projected contact area that is evaluated in terms of the contact depth (h_C) by:

$$\begin{aligned} A_C &= A(h_C) \\ &= 24.5h_C^2 + C_1 24.5h_C^1 + C_2 24.5h_C^{\frac{1}{2}} + C_3 24.5h_C^{\frac{1}{4}} \\ &\quad + \dots + C_8 24.5h_C^{\frac{1}{128}} \end{aligned} \quad (4c)$$

where C_1 to C_8 are constants, which have been computed from the calibration of the nanomechanical setup, S is the slope of the load-displacement

Table IV. The hydrogen permeation parameters calculated from the decay transients

Parameters/specimen	$D_L \times 10^{-7}$ ($\text{cm}^2 \text{ s}^{-1}$)	$C_{\text{Lattice}} \times 10^{-7}$ (mol H cm^{-3})	$C_{T_{\text{rev}}} \times 10^{-7}$ (mol H cm^{-3})	$C_{\text{diff}} \times 10^{-7}$ (mol H cm^{-3})	$N_{T_{\text{rev}}} \times 10^{17}$ (cm^{-3})
Untreated	2.25 ± 0.25	5.55 ± 0.55	5.52 ± 0.99	11.07 ± 1.54	6.66 ± 1.19
c-PEN-treated	2.03 ± 0.13	4.46 ± 0.47	3.38 ± 0.55	7.84 ± 1.01	4.08 ± 0.66

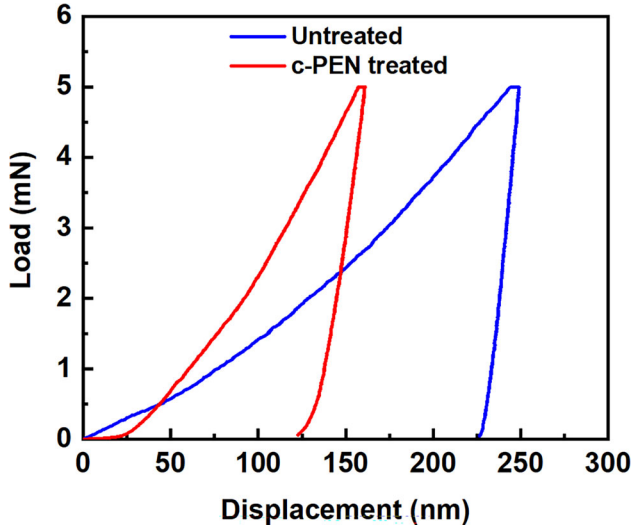


Fig. 6. The load–displacement curves for a 5-mN applied load for a loading rate of 1 mN/s on untreated and c-PEN-treated steel specimens.

curve at the initial unloading, and β is a correction factor that depends on the indenter tip geometry (1.034 for a Berkovich indenter).

The contact depth (h_c) for both the untreated and c-PEN-treated surfaces is quantified in Table V. The c-PEN-treated surface had a smaller contact depth (143.15 nm) compared to the untreated surface (236.03 nm), suggesting that the treated surface exhibited a higher resistance to deformation (Table V). Next, using Eq. (4), the hardness (H) and reduced elastic modulus (E_r) were quantified for both the scenarios. The c-PEN-treated surface was found to be significantly harder (5.81 GPa) compared to the untreated steel surface (2.68 GPa). Furthermore, the reduced elastic modulus for the c-PEN-treated surface was higher (200.39 vs. 184.68 GPa). In the past,²⁶ a similar increment in hardness was observed for nitrided steel compared to untreated steel surface. The observed higher nanomechanical properties for the c-PEN-treated surface can be attributed to the presence of the iron nitride and expanded ferrite phases (Fig. 1).

Analysis of Tribological Properties

Next, the effect of c-PEN treatment on the wear resistance was evaluated by quantifying the variation in coefficient of friction as a function of time (Fig. 7a), obtained using the dry sliding wear test. The coefficient of friction as a function of time was

noticeably lower for the c-PEN-treated specimen (0.47 ± 0.04) than for the untreated steel substrate (0.61 ± 0.05), which was calculated from the stable region of the curve (Fig. 7a). It was reported that the presence of a $\text{FeN}_{0.076}$ phase reduces the coefficient of friction.²⁹ The effect of c-PEN treatment on the wear behavior was further examined by observing the surface topology using an optical profilometer. The c-PEN-treated specimen had a narrower and shallower wear profile compared to the untreated specimen (Fig. 7b2–c2). Furthermore, the estimated wear rate for the c-PEN-treated surface ($3.00 \times 10^{-5} \text{ mm}^3/\text{N m}$) was nearly two times lower than for the untreated specimen ($6.44 \times 10^{-5} \text{ mm}^3/\text{N m}$) (refer to online supplementary material Fig. S-1).

Based on the SEM characterization (Fig. 7b3–c3) of the wear surfaces, it was found that the wear took place by predominantly plastic deformation in both the untreated and c-PEN-treated specimens. In the case of the untreated specimens, the debris in the wear track forms deep scratches because of continuous sliding, resulting in a higher coefficient of friction and wear rate (Fig. 7b). In the case of the c-PEN-treated specimen, the wear debris plastically deforms and flows away from the wear track, as postulated by Ref. 46 (Fig. 7c). Furthermore, in the case of the c-PEN treated specimen, it is plausible that, during the wear test, the increase in local temperature at the wear track leads to an increase in the oxidative wear, which can be attributed to the observed decrease in the wear rate compared to the untreated surface, similar to the conclusions drawn in Ref. 47, which were corroborated with the help of EDS mapping of oxygen on the wear surface. To elaborate, in the case of the untreated specimen, a higher concentration of oxygen was found at the wear track, indicating the oxidation of the wear debris that were compacted on the wear track (Fig. 7b4). On the other hand, in the case of the c-PEN-treated specimen, an oxygen-rich region was found outside the wear track, corresponding to the oxidized wear particles deposited during plastic deformation (Fig. 7c4). Moreover, H^3/E_r^2 which is an indicator of the operating wear mechanism, was quantified here (see Table V).⁴⁸ The c-PEN-treated specimen had a H^3/E_r^2 value (0.005 GPa) which is almost an order higher than that of the untreated specimen (0.0006 GPa), thus suggesting a higher amount of plastic deformation of the wear particles in the untreated surface. The effect of applied load and sliding velocity on the wear behavior was also

Table V. The nano-mechanical parameters obtained from the nano-indentation tests

Parameters/ specimen	Contact depth, h_c (nm)	Reduced elastic modulus, E_r (GPa)	Hardness, H (GPa)	H/E_r	H^3/E_r^2 (GPa)
Untreated	236.03	184.68	2.68	0.015	0.0006
c-PEN-treated	143.15	200.39	5.81	0.029	0.005

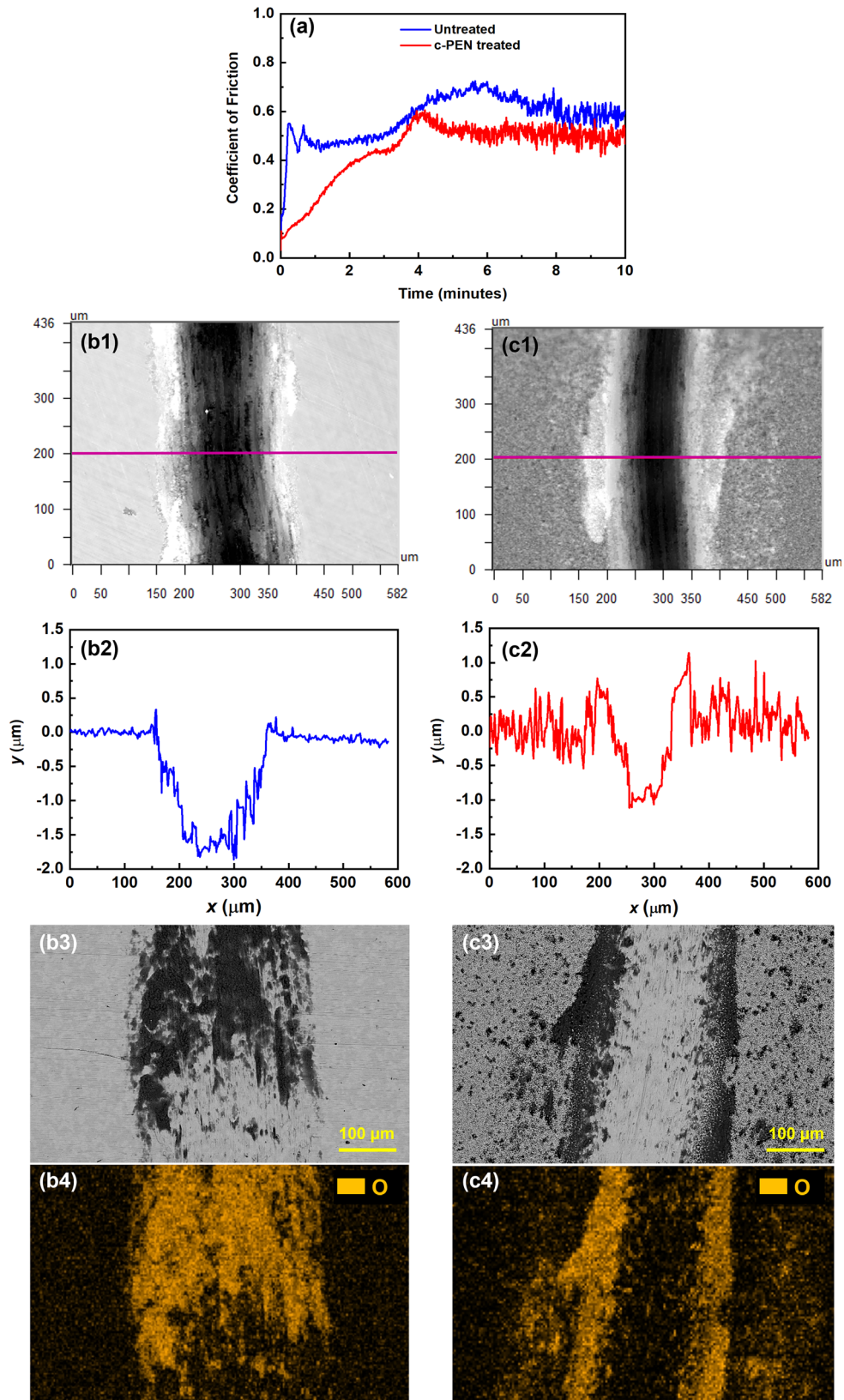


Fig. 7. (a) The coefficient of friction as a function of sliding time for untreated and c-PEN-treated specimens. A representative surface image for both the untreated (b1) and treated (c1) specimens after the wear test. (b2, c2) The cross-sectional profiles at the marked section for the untreated and c-PEN treated specimen. (b3, c3) SEM micrographs for both the specimens after the completion of the wear test. The EDS area mapping of oxygen on the worn surfaces of the untreated (b4) and c-PEN-treated (c4) specimens, respectively.

examined (refer to online supplementary material). Overall, it was found that, at higher applied load (3 N) and sliding velocity (0.2 m/s), the c-PEN-treated layer was ineffective in mitigating wear. However, these can be addressed in future work by optimizing the c-PEN treatment parameters to obtain a thicker deposition layer, which can provide better tribological performance. These findings clearly demonstrated the enhanced wear resistance of the steel after c-PEN treatment, which can be attributed to the presence of a harder c-PEN layer. Furthermore, at the microscopic scale, the saturation of N atoms into the ferrite matrix and the grain boundaries, along with the presence of a FeN_{0.076} phase in the c-PEN layer, leads to the observed wear behavior.

CONCLUSION

A cathodic plasma electrolytic nitriding technique was utilized to modify the 2.25Cr-1Mo ferritic steel surface. The modified surface layer was microscopically analyzed, confirming that the nitride layer (c-PEN layer) was formed successfully during the process. Then, the corrosion and hydrogen permeation properties of the steel were examined for both c-PEN-treated and untreated steel to study the effect of the c-PEN treatment. Furthermore, the wear performance was evaluated to suggest a plausible wear mechanism. The following conclusions are drawn from the present study:

1. The XRD analysis of the c-PEN-treated steel showed lattice expansion of the BCC-ferrite phase due to the supersaturation of nitrogen in the lattice and the presence of the FCC-iron nitride phase in the c-PEN layer.
2. The electrochemical studies in 3.5% NaCl solution showed that the c-PEN-treated steel exhibits a nobler corrosion potential (− 0.47 V vs. Ag/AgCl) than the untreated steel (− 0.58 V vs. Ag/AgCl). It can be thus inferred that the corrosion inhibition performance of the steel was improved by the c-PEN treatment.
3. Hydrogen permeation tests revealed that the hydrogen permeation resistance properties were enhanced by the reduction of hydrogen diffusivity and permeability in c-PEN-treated steel in comparison to the untreated steel. The permeability of the c-PEN-treated steel was reduced to 27%. Also, the reduction in reversible trap density with less hydrogen diffusivity showed that the hydrogen embrittlement susceptibility of the steel was reduced by the c-PEN treatment.
4. The tribological characterization of the c-PEN-treated steel found that the wear predominantly took place through plastic deformation, where the wear particles flowed outside the wear track and were deposited on the wear track. Furthermore, for an applied load of 1 N and a sliding velocity of 0.1 m/s, the c-PEN-treated layer

exhibited an improved tribological performance, based on the observed lower wear rate and coefficient of friction.

It should be noted that the performance of the c-PEN-treated surface in ferritic steels can be optimized for a specific application (corrosion, hydrogen permeation barrier, tribological, and hardness). Overall, this work highlights the multi-functional potential of the c-PEN surface modification technique in ferritic steels to improve the applicability in extreme conditions.

SUPPLEMENTARY INFORMATION

The online version contains supplementary material available at <https://doi.org/10.1007/s11837-023-05988-z>.

ACKNOWLEDGEMENTS

RC, IA, and LN acknowledge the support of IIT Madras through the Institute of Eminence Grant (SB/2021/0992/MEMHRD/008517). Furthermore, RC and IA acknowledge the support from the Department of Science and Technology, India under the early career research award (Program Contract ECR/2018/001100).

CONFLICT OF INTEREST

The authors declare that they have no known competing financial interests or personal relationships that could have appeared to influence the work reported in this paper.

REFERENCES

1. P.C. Siquara, C.B. Eckstein, L.H. de Almeida, and D.S. dos Santos, *J. Mater. Sci.* 42, 2261 (2007).
2. S. Pillot, C. Chauvy, S. Corre, L. Coudreuse, A. Gingell, D. Héritier, and P. Toussaint, *Int. J. Press. Vessels Pip.* 110, 17 (2013).
3. L.R.O. Costa, L.F. Lemus, and D.S. dos Santos, *Int. J. Hydrog. Energy* 40, 17128 (2015).
4. H. Kovacı, O. Baran, A.F. Yetim, Y.B. Bozkurt, L. Kara, and A. Çelik, *Surf. Coat. Technol.* 349, 969 (2018).
5. M. Morcillo, B. Chico, I. Díaz, H. Cano, and D. de la Fuente, *Corros. Sci.* 77, 6 (2013).
6. N. Parvathavarthini, S. Saroja, R.K. Dayal, and H.S. Khatak, *J. Nucl. Mater.* 288, 187 (2001).
7. T. Jonsson, N. Folkesson, J.-E. Svensson, L.-G. Johansson, and M. Halvarsson, *Corros. Sci.* 53, 2233 (2011).
8. M.R. Danelon, L.S. de Almeida, M.D. Manfrinato, and L.S. Rossino, *Surf. Interfaces* 36, 102352 (2023).
9. Y. Fan, W. Liu, W. Yang, Y. Zhao, B. Dong, L. Chen, and T. Zhang, *J. Mater. Eng. Perform.* (2022).
10. D. Hejazi, A.J. Haq, N. Yazdipour, D.P. Dunne, A. Calka, F. Barbaro, and E.V. Pereloma, *Mater. Sci. Eng. A* 551, 40 (2012).
11. K. Takasawa, R. Ikeda, N. Ishikawa, and R. Ishigaki, *Int. J. Hydrog. Energy* 37, 2669 (2012).
12. B. Beidokhti, A.H. Koukabi, A. Dolati, and P. He, *Int. J. Mod. Phys. B* 23, 1209 (2009).

13. X. Zuo, and Z. Zhou, *Mater. Res.* 18, 36 (2015).
14. H. Kovacı, Y.B. Bozkurt, A.F. Yetim, M. Aslan, and A. Çelik, *Surf. Coat. Technol.* 360, 78 (2019).
15. Q. Zeng, J. Sun, W. Emori, and S.L. Jiang, *J. Mater. Eng. Perform.* 25, 1773 (2016).
16. H. Shen, and L. Wang, *Surf. Coat. Technol.* 403, 126390 (2020).
17. M. Bianco, S. Poitel, J.-E. Hong, S. Yang, Z.-J. Wang, M. Willinger, R. Steinberger-Wilckens, and J. Van Herle, *Corros. Sci.* 165, 108414 (2020).
18. H. Kovacı, Y.B. Bozkurt, A.F. Yetim, Ö. Baran, and A. Çelik, *Tribol. Int.* 156, 106823 (2021).
19. H. Kovacı, and Y. Seçer, *Surf. Coat. Technol.* 400, 126178 (2020).
20. P. Bruzzoni, S.P. Brühl, B.J.A. Gómez, L. Nosei, M. Ortiz, and J.N. Feugeas, *Surf. Coat. Technol.* 110, 13 (1998).
21. J.J.M. Jebaraj, D.J. Morrison, J.B. McLaughlin, and I.I. Suni, *J. Electrochem. Soc.* 161, C261 (2014).
22. Z. Wolarek, and T. Zakroczymski, *Acta Mater.* 52, 2637 (2004).
23. J. Huang, H. Xie, L. Luo, X. Zan, D. Liu, and Y. Wu, *Surf. Coat. Technol.* 383, 125282 (2020).
24. X. Nie, L. Wang, Z.C. Yao, L. Zhang, and F. Cheng, *Surf. Coat. Technol.* 200, 1745 (2005).
25. A. Roy, R.K. Tewari, R.C. Sharma, and R. Shekhar, *Surf. Eng.* 23, 243 (2007).
26. J.H. Kong, M. Okumiya, Y. Tsunekawa, T. Takeda, K.Y. Yun, M. Yoshida, and S.G. Kim, *Surf. Coat. Technol.* 232, 275 (2013).
27. S.A. Kusmanov, A.A. Smirnov, Yu.V. Kusmanova, and P.N. Belkin, *Surf. Coat. Technol.* 269, 308 (2015).
28. I.G. Dyakov, S.V. Burov, P.N. Belkin, E.V. Rozanov, and S.A. Zhukov, *Surf. Coat. Technol.* 362, 124 (2019).
29. T. Zhang, J. Wu, L. Jin, Z. Zhang, W. Rong, B. Zhang, Y. Wang, Y. He, W. Liu, and X. Li, *J. Mater. Sci. Technol.* 35, 2630 (2019).
30. S.A. Kusmanov, I.V. Tambovskii, S.S. Korableva, S.A. Silkin, A.A. Smirnov, I.A. Kusmanova, and I.S. Gorokhov, *Surf. Eng. Appl. Electrochem.* 58, 323 (2022).
31. P.N. Belkin, A. Yerokhin, and S.A. Kusmanov, *Surf. Coat. Technol.* 307, 1194 (2016).
32. *R. Proc. Soc. Lond. Ser. Math. Phys. Sci.* 270, 90 (1962).
33. W.C. Oliver, and G.M. Pharr, *J. Mater. Res.* 7, 1564 (1992).
34. G02 Committee, *Test Method for Wear Testing with a Pin-on-Disk Apparatus* (ASTM International, n.d.).
35. S.A. Kusmanov, I.V. Tambovskiy, V.S. Sevostyanova, S.V. Savushkina, and P.N. Belkin, *Surf. Coat. Technol.* 291, 334 (2016).
36. A.P. Tschiptschin, L.B. Varela, C.E. Pinedo, X.Y. Li, and H. Dong, *Surf. Coat. Technol.* 327, 83 (2017).
37. W. Gui, J. Lin, G. Hao, Y. Qu, Y. Liang, and H. Zhang, *Sci. Rep.* 7, 308 (2017).
38. A. Barnoush, M. Asgari, R. Johnsen, and R. Hoel, *Metall. Mater. Trans. A* 44, 766 (2013).
39. K.S. Reddy, Y. Govindaraj, and L. Neelakantan, *J. Mater. Sci.* 57, 19592 (2022).
40. ASTM G148-97(2018), *Practice for Evaluation of Hydrogen Uptake, Permeation, and Transport in Metals by an Electrochemical Technique* (ASTM International, n.d.).
41. K.S. Reddy, Y. Govindaraj, and L. Neelakantan, *Electrochim. Acta* 439, 141727 (2023).
42. T. Zakroczymski, J. Flis, N. Lukomski, and J. Mankowski, *Acta Mater.* 49, 1929 (2001).
43. O. Barrera, D. Bombac, Y. Chen, T.D. Daff, E. Galindo-Nava, P. Gong, D. Haley, R. Horton, I. Katzarov, J.R. Ker-mode, C. Liverani, M. Stopher, and F. Sweeney, *J. Mater. Sci.* 53, 6251 (2018).
44. Q. Liu, J. Venezuela, M. Zhang, Q. Zhou, and A. Atrens, *Corros. Sci.* 111, 770 (2016).
45. B.A. Szost, R.H. Vegter, and P.E.J. Rivera-Díaz-del-Castillo, *Metall. Mater. Trans. A* 44, 4542 (2013).
46. A. Matthews, S. Franklin, and K. Holmberg, *J. Phys. Appl. Phys.* 40, 5463 (2007).
47. T. Polcar, N.M.G. Parreira, and A. Cavaleiro, *Wear* 262, 655 (2007).
48. X. Chen, Y. Du, and Y.-W. Chung, *Thin Solid Films* 688, 137265 (2019).

Publisher's Note Springer Nature remains neutral with regard to jurisdictional claims in published maps and institutional affiliations.

Springer Nature or its licensor (e.g. a society or other partner) holds exclusive rights to this article under a publishing agreement with the author(s) or other rightsholder(s); author self-archiving of the accepted manuscript version of this article is solely governed by the terms of such publishing agreement and applicable law.